MDPI

Evolution of Ternary AuAgPd Nanoparticles by the Control of Temperature, Thickness, and Tri-Layer

Sundar Kunwar [1], Puran Pandey [1], Mao Sui [1], Sushil Bastola [1] and Jihoon Lee [1,2,*]

[1] College of Electronics and Information, Kwangwoon University, Seoul 01897, South Korea;
kunwarankees23@gmail.com (S.K.); ppcpurans@gmail.com (P.P.); maosui001@163.com (M.S.);
lisusdrimz@gmail.com (S.B.)

[2] Institute of Nanoscale Science and Engineering, University of Arkansas, Fayetteville, AR 72701, USA

[*] Correspondence: jihoonleenano@gmail.com; Tel.: +82-2-940-5297

Abstract: Metallic alloy nanoparticles (NPs) possess great potential to enhance the optical, electronic, chemical, and magnetic properties for various applications by the control of morphology and elemental composition. This work presents the fabrication of ternary AuAgPd alloy nanostructures on sapphire (0001) via the solid-state dewetting of sputter-deposited tri-metallic layers. Based on the systematic control of temperature, thickness, and deposition order of tri-layers, the composite AuAgPd alloy nanoparticles (NPs) with various shape, size, and density are demonstrated. The metallic tri-layers exhibit various stages of dewetting based on the increasing growth temperatures between 400 and 900 °C at 15 nm tri-layer film thickness. Specifically, the nucleation of tiny voids and hillocks, void coalescence, the growth and isolated nanoparticle formation, and the shape transformation with Ag sublimation are observed. With the reduced film thickness (6 nm), tiny alloy NPs with improved structural uniformity and spatial arrangement are obtained due to enhanced dewetting. The growth trend of alloy NPs is drastically altered by changing the deposition order of metallic tri-layers. The overall evolution is governed by the surface diffusion and inter-mixing of metallic atoms, Rayleigh-like instability, surface and interface energy minimization, and equilibrium state of the system. The UV-VIS-NIR reflectance spectra reveal the formation of an absorption band and reflectance maxima at specific wavelengths based on the morphology and composition of AuAgPd alloy NPs. In addition, Raman spectra analysis shows the modulation of intensity and peak position of natural vibration modes of sapphire (0001).

Keywords: AuAgPd alloys; solid-state dewetting; alloy nanoparticles; sapphire (0001); plasmonics

1. Introduction

Multi-metallic alloy NPs have garnered considerable research interest because of their wide range of structural and elemental tunability and functional diversity, making them applicable in many nanodevices and -technologies [1–6]. In addition, the electronic heterogeneity, site-specific response, and combinational effect of constituent metals are some interesting features of the alloy NPs, which could not be achieved with monometallic NPs. At the same time, the alloy NPs can provide additional flexibility for tuning optical [7,8], catalytic [9–13], electronic, and magnetic [14–16] properties by controlling shape, size, and density [17] as well as elemental composition. In particular, the localized surface plasmon resonance (LSPR) frequency of alloy NPs can be modulated through the composition variation, which potentially enables many applications in the plasmonic, energy, and biomedical fields. For instance, the durability of Pd-based nanocatalysts has been significantly improved by the addition of Au in the NPs [18] and the incorporation of Pd into Ag NPs can demonstrate a red shift of plasmon resonance peak from 440 to 732 nm along with the increased Pd composition [19]. In recent years, monometallic Au, Ag, and Pd NPs have been successfully utilized in many fields

owing to their promising plasmonic and catalytic properties; therefore, the fabrication of AuAgPd alloy NPs can offer novel application as well as improved performance of existing applications [20–22]. The systematic fabrication of ternary AuAgPd alloy NPs with tunable surface morphology and elemental composition, however, has not been reported in the literature. In this study, the AuAgPd alloy NPs' growth is demonstrated on c-plane sapphire (0001) via the solid-state dewetting of tri-metallic thin films. The solid-state dewetting is a process of transformation of a continuous thin film into isolated particles or droplets by means of atomic diffusion, which has been extensively used to fabricated substrate-supported nanostructures [17,23]. The atomic diffusion can initiate the dewetting process by the nucleation of holes in the film upon heating. Then, along with elevated temperature or time of heating, the holes grow larger due to the hole edge retraction, resulting in the formation of ligaments and finally of particles due to the Rayleigh-like instability. The overall transformation occurs at solid state, which is driven by the energy minimization of the thermodynamic system. The structure, shape, size, and orientation of the resulting nanostructures mainly depend upon the initial film thickness, temperature, and duration of annealing. Therefore, in this work, controlled thermal energy is employed to induce the successful dewetting of sputter-deposited tri-metallic thin films below the melting temperature. Depending upon the annealing temperature, initial film thickness, and deposition sequence, various composite alloy NPs are obtained, which are discussed based on the related growth mechanism and models. The surface morphologies, elemental composition, and optical properties are investigated by using atomic force microscope (AFM), a scanning electron microscope (SEM), an energy-dispersive X-ray spectroscope (EDS), and reflectance spectroscopy, correspondingly.

2. Materials and Methods

2.1. Substrate Preparation and Fabrication

Sapphire (0001) wafers used in this work were ~430 μm thick with $\pm 0.1°$ off-axis (iNexus Inc., Seoul, South Korea). Initially, sapphire wafers were diced into square pieces (6×6 mm^2) using a mechanical saw. Degassing was performed at 900 °C for 30 min under 1×10^{-4} Torr in a pulsed laser deposition (PLD) chamber. The surface contaminants, dust particles, and oxide particles were expected to be removed and a smooth surface texture was observed by AFM scanning after degassing, as shown in Figure A1a,b. In addition, the Raman characteristic showed six active phonon modes that resemble the natural phonon modes of sapphire, as shown in Figure A1c. Then, metal layers of Au, Ag, and Pd were sequentially deposited on sapphire (0001) from high-purity (99.999%) metal targets using plasma sputtering. The deposition condition was identical for all metal layers with a deposition rate of 0.01 nm·s^{-1} and ionization current of 5 mA under 1×10^{-1} Torr chamber pressure. In the first set, Au, Ag, and Pd layers were sequentially deposited with a 5 nm thickness of each layer (Au/Ag/Pd). Similar deposition order of Au/Ag/Pd with 6 nm total thickness (2 nm of each layers) was also prepared to study the effect of a lower thickness. Furthermore, the deposition order was altered to Pd/Au/Ag with 6 nm total thickness to observe the deposition order effect. Following the deposition of metallic multilayers, samples were transferred to a PLD chamber for annealing at various temperatures between 400 and 900 °C. For the growth of nanostructures at specific temperatures, individual samples were annealed. In order to maintain the consistency, the annealing process was controlled by computer-operated recipes and the target temperature was attained at a ramping rate of 4 °C·s^{-1}. After reaching the target temperature, the dwelling duration of 450 s was equally applied for each sample. To finish the fabrication, the heating system was turned off and samples were kept inside a vacuum until the temperature dropped to ambient.

2.2. Characterization

The surface morphologies of as-fabricated AuAgPd alloy NPs were studied using an atomic force microscope (AFM, Park Systems, Seoul, South Korea) and a scanning electron microscope (SEM, CoXEM, Seoul, South Korea). The surface arrangement, configuration, dimension, and density of

NPs were extracted from AFM images and large-scale surface morphologies were studied by SEM images. The results were analyzed in terms of cross-sectional line profiles, FFT power spectra, 3D side-views, roughness, and surface area ratio. The elemental analysis of the alloy NSs were performed by an energy dispersive X-ray spectroscope (EDS, Thermo Fisher, Noran System 7, Waltham, MA, USA). The Raman and reflectance spectra were measured with a UNIRAM II system (UniNanoTech Co. Ltd., Seoul, South Korea) equipped with ANDOR sr-500 spectrograph, CCD detector, and various pieces of optical equipment. Combined halogen and deuterium lamps (OCEAN Optics, Largo, FL, USA) and a 532 nm CW diode-pumped solid-state (DPSS) laser at 220 mW were utilized for reflectance and Raman spectra, respectively.

3. Results and Discussion

Figure 1 shows a general depiction of AuPdAg alloy NPs fabrication on sapphire (0001) based on the temperature control along with the different evolution stages. The alloy NPs were fabricated at various temperatures between 400 and 900 °C for 450 s. As shown in Figure 1a, the metal tri-layers consisted of Au, Ag, and Pd layers in the order of Au/Ag/Pd with 5 nm individual layer thickness, for a total thickness of 15 nm. The growth of alloy NPs can be divided into two steps: (i) void and nanocluster evolution, and (ii) nanoparticle evolution. The formation of multi-metallic alloy NPs from the Au/Ag/Pd tri-layers can be discussed based on the solid state dewetting of thin films by means of surface and interface diffusion at elevated temperature, as shown in Figure 1b. Generally, the sputter-deposited metallic thin films can be unstable or meta-stable, which can be transformed into individual particle of the certain configuration with the appropriate annealing. The deposited atoms can be activated by the applied thermal energy and diffusion through the surface and interface of distinct metal layers (inter-mixing) can be induced. The diffusion coefficient (D_S) of atoms and temperature can be related as follows: $D_S \propto exp\left(-\frac{E_{ai}}{kT}\right)$, where E_{ai} is the activation energy, K is the Boltzmann constant, and T is the annealing temperature. In response to sufficient diffusion, voids/pinholes can be perforated at the low energy sites in the thin films: i.e., at misfit dislocations, triple junctions, grain boundaries, and steps on substrates [18]. Then, along with the temperature increment, the diffusion and inter-mixing of atoms can be enhanced through the pinholes. Consequently, once the voids are formed, they start to grow larger by merging with nearby ones due to the capillary forces around void rims/edges, as shown in Figure 1c. Therefore, the dewetting can be progressively enhanced by the void growth and ligament formation due to the instability of retracting edges. Finally, the breakdown of ligaments can occur due to Rayleigh-like instability resulting in the formation of isolated NPs [23]. At the same time, owing to the stronger binding energy between metallic atoms than with sapphire atoms, the 3D growth of alloy NPs occurs based on the Volmer–Weber growth model, as displayed in Figure 1d. Furthermore, the inter-mixing of atoms depends on the system temperature, and therefore the elemental distribution of Au, Ag, and Pd within alloy NPs can be improved with temperature. The solid-state dewetting process depends largely on the substrate temperature, film thickness, chemical potential, surface and interface energies, and substrate properties [24,25]. In the multilayer system, each metal layer possesses different thermal expansion coefficient, surface energy, and diffusivity, and thus the dewetting process of multilayers can be more complex as compared to the monometallic film. For example, the surface energies of Au, Ag, and Pd are 1363, 1065, and 1808 mJ·m^{-2}, respectively, which indicates that Ag has the highest surface diffusion, followed by Au and Pd [26]. Previous results clearly showed the distinct dewetting behavior of Au, Ag, and Pd metal layers on various substrates. Generally, Ag layers have shown significant dewetting around 400 °C, whereas Au and Pd demonstrated visible dewetting above 500 and 600 °C, respectively [27–29]. On the other hand, the interaction force between metal film and substrate will also play an important role in the dewetting process, such that the interaction force of Pd-sapphire is higher than Au-sapphire, which will be discussed in the later section on altered tri-layer deposition. Nevertheless, the overall dewetting process is driven by the surface and interface energy minimization of the thermodynamic system. In the case of Au, Ag, and Pd, they all possess an fcc crystallographic

structure with complete miscibility, and thus the composite AuAgPd alloy nanostructures can be fabricated by sufficient dewetting and inter-mixing at a certain temperature [30]. Previous studies have shown the fully inter-mixed AuAgPd alloy NPs from the evaporation deposited tri-layers of ~25 nm thickness by heating to ~500 °C [31]. The surface morphology of the as-deposited (Figure A2) uniform tri-layers was gradually transformed by the evolution of voids and nanoclusters at a relatively low temperature, and then isolated NPs at high temperature, as seen in Figure 1c,d. The detailed analysis of the AuAgPd alloy NP formation is presented in Figure 2. As shown in Figure 2a, at 400 °C, tiny voids or pinholes were perforated on the film surface as an initial stage of dewetting at a relatively low temperature. Meanwhile, a few large nanoclusters already developed around the void rims because the diffusion of atoms can be enhanced through the void edges, as discussed earlier [32]. At this stage, the inter-mixing of metal atoms might not be sufficient and thus the partially dewetted nanoclusters might consist of an inhomogeneous distribution of Au, Ag, and Pd atoms. When the temperature was increased to 600 °C, the voids extended due to the retraction of void rims along with enhanced surface diffusion. Specifically, the typical void width increased from ~50 nm to above 150 nm between 400 and 600 °C, which can be clearly observed in the cross-sectional line profiles in Figure 2(a-1–c-1). The void expansion and coalescence with the neighboring ones can be driven by the interfacial energy minimization between the film and substrate [33]. Subsequently, large nanoclusters were formed due to the enhanced diffusion and inter-mixing of Au, Pd, and Ag atoms at a high temperature. For example, between 700 and 900 °C, the transformation of irregularly connected nanoclusters into isolated NPs was observed due to the Rayleigh-like instability of connected ligaments [34]. Consequently, the isolated NPs developed into a more regular and compact configuration along with the increased temperature, as shown in Figure 2d–f. More specifically, between 800 and 900 °C, the evolution of alloy NPs mainly occurred as the shape transformation and number of irregular and wiggly NPs were gradually reduced, whereas the number of semi-spherical NPs increased. The evolution of semi-spherical NPs can be due to the tendency to achieve an isotropic surface energy distribution in order to gain thermodynamic stability with reduced surface energy [27,35]. The cross-section line profiles of the typical alloy NPs clearly demonstrated a dome-shaped rim, as shown in Figure 2(e-1,f-1). The surface morphologies of large nanoclusters and isolated alloy NPs were further inspected by large-scale SEM images, shown in Figure 2(d-2–f-2). Moreover, the surface modulation was studied by the roughness and surface area ratio (SAR), as shown in Figure 2g,h. The roughness parameters; root mean square roughness (Rq), and average roughness (Ra) are given as: $Ra = \frac{1}{n}\sum_1^n |Zn|$ and $= \sqrt{\frac{1}{n}\sum_1^n Z_n^2}$, where Zn is the height profile at each pixel. Both Rq and Ra were amplified with the temperature, indicating the average height growth due to the formation of nanoclusters and subsequent NPs. In terms of SAR, the percentile increment of surface area is: $= \frac{A_g - A_s}{A_g} \times 100\%$, where A_g and A_s are the geometric (2D) and surface area (3D), respectively. The SAR also increased as the 3D surface area of alloy nanostructures was enlarged with temperature. The elemental analysis of each sample was performed by EDS spectra measurement. The full EDS spectrum range in Figure 3a shows the elements present in the samples at 400 °C and the insets display Ag- and Pd-related peaks at 400 and 900 °C. The EDS count corresponds to the Au Mα1, Ag Lα1, and Pd Lα1 peaks, summarized in a plot in Figure 2i. Generally, Ag Lα1 peak counts are higher in comparison with Ag Lα1 and Pd Lα1 peak counts due to the higher atomic number of Au. From the EDS counts of elements, Au and Pd were found to vary slightly within the error range throughout the temperature; however, Ag gradually decreased above 600 °C. This indicates that Ag sublimation occurred significantly above 600 °C and the sublimation rate escalates along with the temperature [28,29]. Therefore, the evolution of alloy NPs at high temperature can also be affected by the Ag sublimation, such that we see size reduction and shape transformation. The sublimation loss of Ag in this case was much lower compared to the pure Ag nanoparticles due to the inter-mixing with Au and Pd [29]. Furthermore, the atomic homogeneity of metal elements can improve with increased temperature, exceeding the melting point, as observed in previous results [36]; however, Ag can be extensively sublimated.
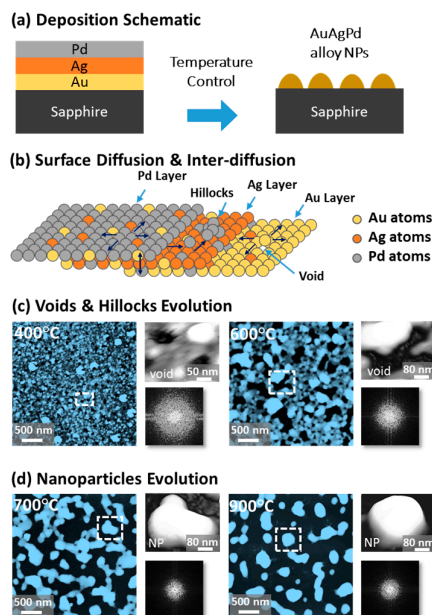
Figure 1. Evolution of ternary AuAgPd NPs on sapphire (0001), annealed between 400 and 900 °C for 450 s with 15 nm total thickness. (**a**) Tri-layer deposition schematic showing the deposition sequence of Au, Ag, and Pd layers (Au:Ag:Pd = 1:1:1). (**b**) Illustration of surface diffusion and inter-diffusion between metallic layers. (**c**) Atomic force microscope (AFM) top-views display the voids and nanoclusters evolution at relatively low temperature from 400 and 600 °C. (**d**) Irregular-connected to isolated-dome shaped AuAgPd alloy nanoparticle (NP) evolution between 700 and 900 °C. Corresponding insets present a zoomed-in view of the selected region and Fourier filter transform (FFT) power spectra.
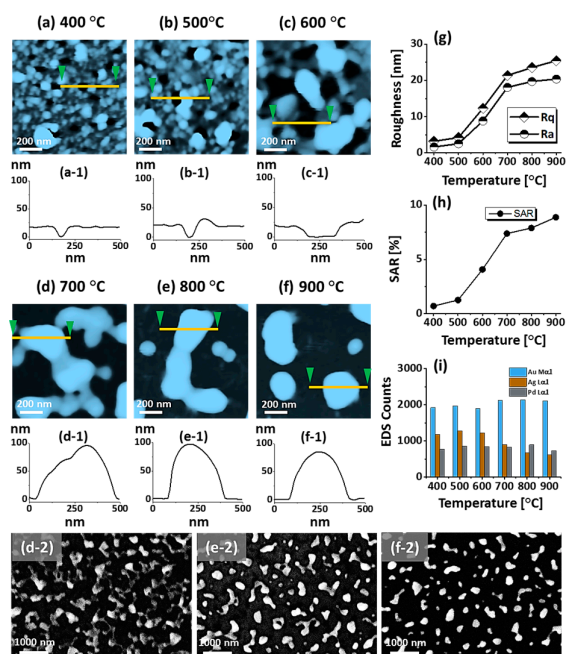
Figure 2. Formation of self-assembled ternary AuAgPd alloy NPs. (**a**–**f**) AFM top-views of 1×1 μm^2 show the gradual evolution of voids, nanoclusters and nanoparticles (NPs) between 400 and 900 °C for 450 s. (**a-1**–**f-1**) Cross-sectional line profiles based on the line in AFM top-views. Summary plot of (**g**) roughness, (**h**) surface area ratio (SAR) and (**i**) energy dispersive *x*-ray spectroscope (EDS) counts with respect to the annealing temperature. (**d-2**–**f-2**) Scanning electron microscope (SEM) images of alloy NPs between 700 and 900 °C.
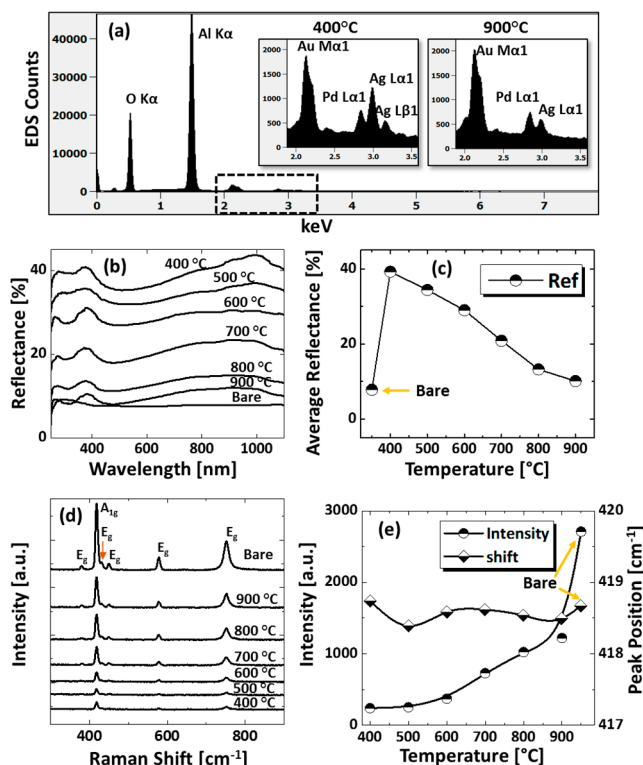
Figure 3. (**a**) EDS spectra between 0 to 7.5 keV of the samples at 400 °C and 900 °C. (**b**) Reflectance spectra of tri-metallic NPs at various temperatures on sapphire (0001) as a function of wavelength. (**c**) Summary plot of average reflectance. (**d**) Raman spectra of the samples. (**e**) Summary plots of peak intensity and peak position with respect to the temperature.

The optical properties were investigated by UV-VIS-NIR reflectance spectroscopy. Figure 3b shows the reflectance spectra for various configurations of AuAgPd alloy NPs on sapphire (0001). The bare sapphire (0001) exhibited an almost flat spectral response, with ~8% average reflectance between 300 and 1100 nm. Depending on the surface morphology evolution of AuAgPd alloy NPs, the reflectance characteristics were significantly modulated. In general, the average reflectance gradually decreased with the elevated temperature, as shown in Figure 3c, in which the average reflectance decreased from ~39% to ~10% when the temperature varied between 400 and 900 °C. This can be correlated to the average surface coverage of sapphire by the alloy nanostructures, as the metallic layer possesses high reflectivity and incident light can be significantly reflected in the case of large surface coverage and vice versa. At the same time, with the formation of definite structure and spacing between NPs, the absorption or scattering effect can be enhanced in the specific wavelength range. For instance, a peak in the UV regime (~380 nm) and a wide shoulder in the NIR regime were commonly observed in all samples. On the other hand, the reflectance was significantly attenuated in the visible region, i.e., ~420–600 nm making a wide dip centered ay ~460 nm, which might be the absorption enhancement due to the surface plasmon resonance of alloy NPs [37–39]. The peak observed in the UV region and NIR region can be due to the quadrupolar and dipolar resonance mode of alloy NPs, respectively, which has been previously observed in the case of pure Ag and Pd NPs [27,29]. The formation of peaks and dips in a similar manner with pure metal NPs indicates that the alloy NPs are composed of well-mixed Au, Ag, and Pd and the optical response collectively contributed by each element. Furthermore, the UV peak and NIR shoulder were gradually weakened, which can be correlated to Ag sublimation, but there was no obvious shift in peak position. The incident light interaction with Ag is stronger as compared with other metal elements; therefore, the LSPR peak intensity decreases with reduced Ag components in alloy NPs. The reflectance spectra of an individual sample and the average reflectance

can be found in Figure A5 and Table A2, respectively. In addition, the Raman spectra of the samples were measured by the excitation of a 532-nm laser from CW diode-pumped solid-state (DPSS) at 220 mW, as shown in Figure 3d. Six vibration modes of sapphire (0001) were commonly observed in all samples, in which the peak at 419 cm^{-1} is due to the A_{1g} and others are due to the E_g vibration modes [40]. The intense vibration mode, i.e., A_{1g} at 419 cm^{-1} was used to characterize the samples based on the peak intensity and peak position. In general, after the fabrication of the AuAgPd alloy NSs, the peak intensity was weakened as compared to the bare sapphire. As summarized in Figure 3e, the peak intensity was lowest at 400 °C and gradually increased with temperature. The peak intensity showed a direct dependency on the average surface coverage by the alloy NPs such that the higher the surface coverage the lower the peak intensity and vice versa. This can be caused by the absorption of the incident laser by the alloy NPs, as suggested by the dip in the visible region of the reflectance spectra. On the other hand, the peak positions were slightly red shifted (<1 cm^{-1}) in all samples except the one at 400 °C, possibly due to the stress that developed between alloy nanostructures and substrate lattice [41]. The specific values of peak intensity and peak position are summarized in Table A3.

Figure 4 presents the evolution of small and dense semi-spherical AuAgPd alloy NPs, fabricated with relatively low film thickness, i.e., 6 nm, which consist of 2 nm Au, Ag, and Pd (Au:Ag:Pd = 1:1:1) in sequential order. The AuAgPd alloy NPs were fabricated in an identical environment as the previous set, i.e., between 400 and 800 °C for 450 s. As compared to the previous set, a sharp distinction of the dewetting process was observed due to the variation of initial film thickness. In general, the alloy NPs exhibited improved uniformity in shape, surface coverage, and spatial homogeneity due to the enhanced dewetting of thin layers. As discussed, the dewetting of the uniform thin film depends on the temperature and thickness [32]. Due to the thinner initial film thickness, significant surface diffusion and inter-diffusion can occur even at a relatively low temperature, leading to the formation of isolated alloy NPs. Generally, voids form when neighboring vacancies or nuclei are coalesced due to the momentum or surface diffusion of the atoms. In the case of thin films, it can be faster with the rapid coalescence of vacancies due to the enhanced surface diffusion of atoms. Therefore, the void nucleation, growth, and accumulation of atoms can be much enhanced with the thinner film thickness, due to which the overall dewetting process can be enhanced. As shown in Figure 4a, at 400 °C, densely packed small alloy NPs were obtained. With the increment of annealing temperature between 600 and 800 °C, the alloy NPs were well-structured by increasing their shape, size, and spacing. Mostly the alloy NPs attained a dome-shaped configuration due to the isotropic surface energy distribution, as discussed earlier. After the formation of isolated NPs, normally NPs can be enlarged in order to gain equilibrium configuration along with enhanced surface diffusion. An enlarged view of alloy NPs along with cross-sectional line profiles is shown in Figure 4(a-3–c-3) and Figure A6. Additionally, the average diameter and height were measured and expressed in terms of histograms, along with the Gaussian distribution curve, as shown in Figure 4(a-1–c-1),(a-2–c-2). As clearly presented by the summary plots, the size of NPs increased significantly between 400 °C and 600 °C, whereas only a minor increment was observed at 800 °C. In addition, the roughness (Rq, Ra) and SAR also showed a similar trend with the temperature. At 800 °C, the dimensional enhancement was not significant, which can be due to the Ag sublimation that may hinder the NPs' growth. The Ag sublimation was confirmed by the EDS spectra analysis, as displayed in Figure 5a. The summary of EDS counts for Au Mα1 and Pd Lα1 was consistent, whereas a gradual reduction of Ag Lα1 counts was observed. Corresponding optical properties were studied by the UV-VIS-NIR reflectance spectra of each sample. The average reflectance was found to decrease with increasing temperature, as presented in Figure 5d, which can be correlated with the enlarged spacing or reduced surface coverage by alloy NPs. On the other hand, there was no significant development of peaks and dips in a specific wavelength region, which is likely due to the broadband absorption of incident light as alloy NPs possessed a smaller size compared to the incident wavelength [42]. Furthermore, the Raman spectra of all samples exhibited six vibration modes of sapphire and the peak intensity and position were probed by the A_{1g} vibration mode.

The peak intensity gradually increased and peak position was slightly red shifted after the fabrication alloy NPs, as summarized in plots in Figure 5e,f.
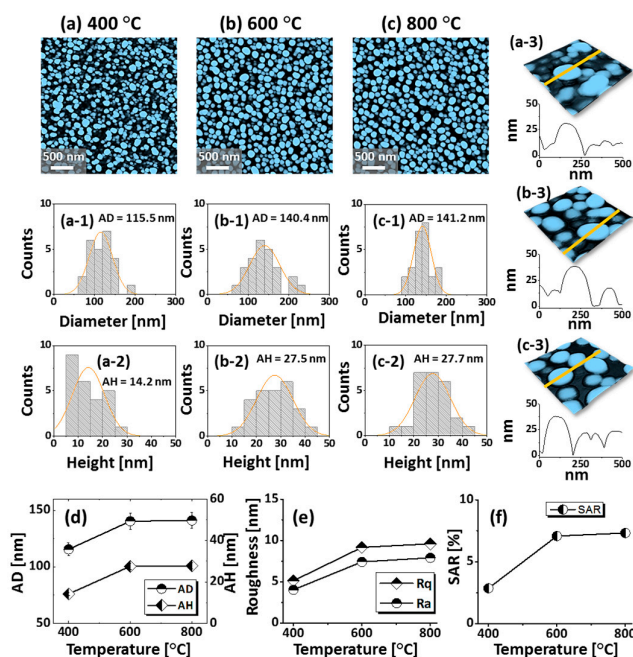

Figure 4. Spherical tiny AuAgPd alloy NPs fabricated with relatively thinner tri-layers (6 nm) by annealing between 400 and 800 °C for 450 s. The tri-layers consisted of 2 nm Au, Ag, and Pd each. (**a–c**) AFM top-views of 3 × 3 μm². (**a-1–c-1**) Diameter distribution histograms. (**a-2–c-2**) Height distribution histograms. (**a-3–c-3**) Enlarged 3D side-views and cross-sectional line profiles. (**d–f**) Summary plots of average diameter (AD), average height (AH), roughness, and SAR.
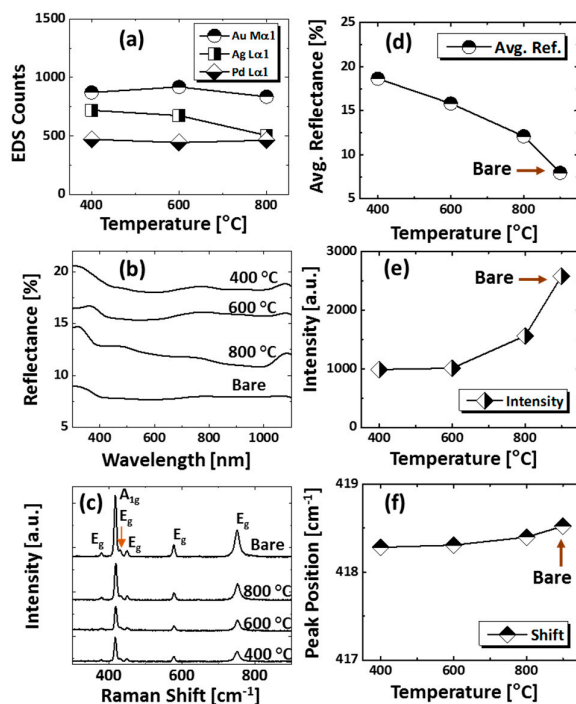
Figure 5. (**a**) EDS peak counts of Au, Ag, and Pd of the samples shown in Figure 4. (**b**) Corresponding reflectance spectra. (**c**) Raman spectra. (**d–f**) Summary plots of average reflectance, Raman intensity, and Raman peak position with respect to the temperature.

Figure 6 presents the fabrication of alloy NPs on the sapphire (0001) by changing the deposition order of tri-layers. Four specific structural configurations of PdAuAg alloy NPs are displayed in terms of 3D side-views in Figure 7a–d at different temperatures. In this case, the tri-layer deposition order was altered to make Pd the first, as shown in the schematic (inset) in Figure 6a, but the growth conditions (400 to 900 °C for 450 s) and total thickness (6 nm) were kept identical. As compared to the previous set, the dewetting process was significantly altered by the variation of deposition order only. For example, a partially dewetted surface morphology was observed at a lower temperature in Figure 7a,b, indicating a hindered diffusion as compared to the previous set, and much larger NPs were formed at a high temperature in Figure 7c,d, indicating enhanced overall diffusion. As the interfacial energies and diffusivities of each metal are distinct from those of sapphire, their dewetting nature and hence the resulting nanostructures can also vary accordingly. For instance, at 400 °C, the nanostructures were mostly connected and irregular, as shown in Figure 6a, and connected nanostructures, partial segmented nanoclusters, and few isolated NPs resulted between 500 and 600 °C. Meanwhile, spherical isolated NPs were observed at 400 °C, with a gradually increased size in the previous set. This may indicate a hindered diffusion in this set, which can be due to the stronger binding energy between Pd-sapphire than Au-sapphire and the lower diffusivity of Pd atoms [43,44]. With the Pd layer being deposited first, it can demonstrate a resistivity or stability to the dewetting at lower temperatures so that partially dewetted structures can be observed. After increasing the temperature to 700 °C, mostly isolated but irregular alloy NPs evolved due to the Rayleigh-like instability of large nanoclusters, as discussed. After the formation of isolated NPs, the shape transformation of alloy NPs was observed up to 900 °C, as shown by the height histograms in Figure 6(a-1–f-1) and summary plots in Figure 6g. Between 700 and 900 °C, the resulting isolated alloy NPs were much larger and the density was much lower as compared to the previous set, which can indicate an enhanced overall diffusion. With the Pd atoms being deposited first, the Pd atoms can create a modified surface matrix by binding with the O atoms in the sapphire matrix due to the higher binding energy [43,44]. Thus, the overall diffusion of well inter-mixed atoms at a high temperature can occur at a modified surface now, such that the dewetting of tri-layers can be enhanced and significantly larger alloy NPs can result with the decreased density. General trends of alloy NPs in this set can also be discussed in terms of the roughness and SAR, as presented in the summary plots in Figure 6h. The average values escalated sharply between 400 and 600 °C, along with the rapid surface evolution of irregular connected NPs; meanwhile, the surface parameter increased mildly between 700 and 900 °C along with the shape transformation. On the other hand, the size enlargement could be hindered by the Ag sublimation at a higher annealing temperature, which likewise can be seen from the EDS count plot in Figure 6i. As a result, only a minor increment in the surface parameters of NPs was observed. Individual EDS spectra are supplied in the appendix. The reflectance measurement of the AuAgPd alloy NPs on sapphire (0001) over the range of 300 to 1100 nm is shown in Figure 7e,f. Along with the evolution of alloy NPs of various configurations, the average reflectance and spectral response varied at different wavelength regimes. In general, the average reflectance was gradually reduced along with the temperature, similar to the previous sets, as shown in Figure 7f. For instance, the average reflectance for the 400 °C sample was ~20%; along with the formation of widely-spaced, smaller and isolated dome-shaped NPs, the average reflectance was gradually attenuated up to ~12% when the temperature reached 900 °C. For the specific peak formation, up to 600 °C, a UV peak at ~380 nm was clear and a wide dip was formed in the visible region in Figure 7e. As the temperature increased above 700 °C, the UV peak and VIS dip gradually vanished. Instead, a clear dip was observed in the NIR region at ~1000 nm with the formation of isolated alloy NPs; this can be correlated to the Ag sublimation, as discussed before.
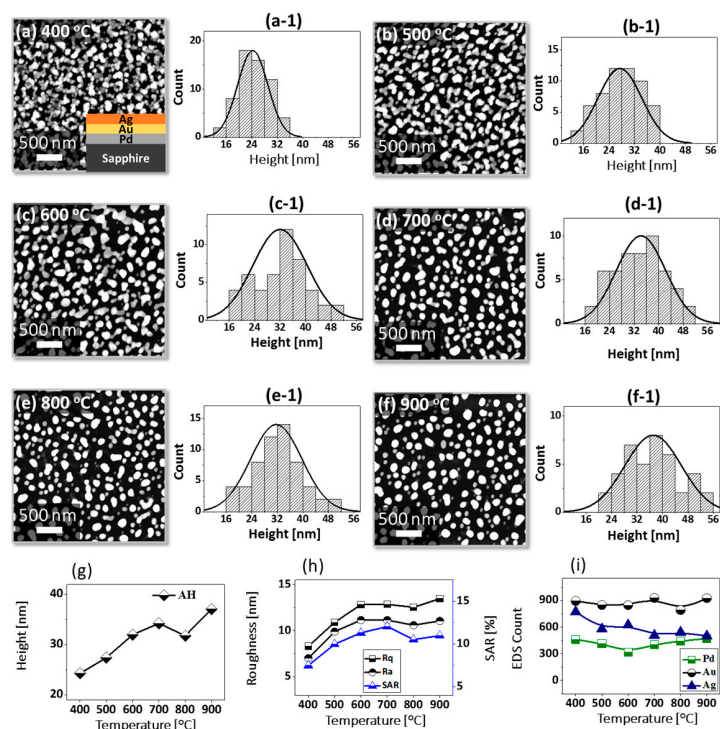
Figure 6. Tri-layer deposition order effect on the evolution of AuAgPd NPs at increased temperature between 400 and 900 °C for 450 s. The tri-layer consisted of 2 nm thick Pd, Au, and Ag layers in sequence (Pd:Au:Ag = 1:1:1), as shown in the inset. (**a**–**f**) AFM top-views of 3 × 3 μm². (**a-1**–**f-1**) Corresponding height distribution histogram. (**g**) Plot of average height (AH) acquired from histogram. (**h**) Plots of Rq, Ra, and SAR. (**i**) Plots of EDS counts corresponding to Au, Ag, and Pd.
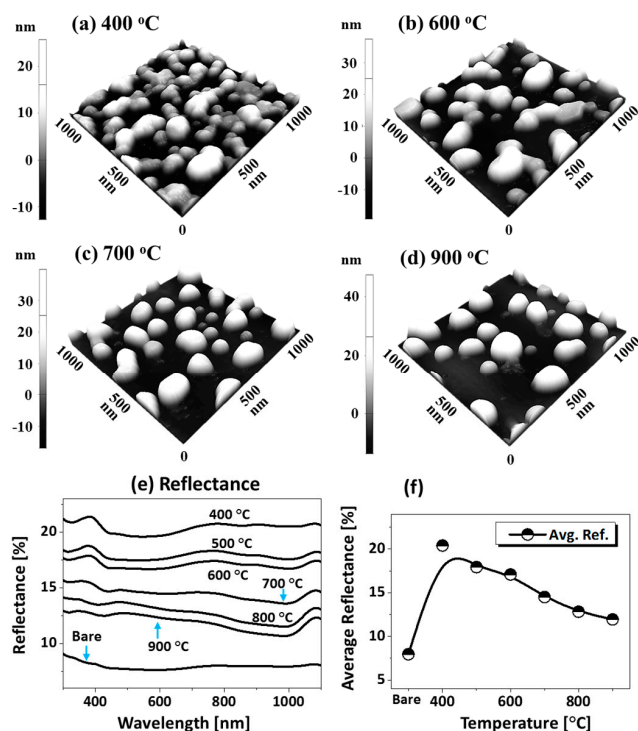
Figure 7. (**a**–**d**) Enlarged side-views of specific samples from Figure 6 showing the typical surface morphology of AuAgPd NPs at different temperatures, as labeled. (**e**) Reflectance spectra. (**f**) Summary of average reflectance with respect to the temperature.

4. Conclusions

In summary, the evolution of various configuration of self-assembled AuAgPd alloy NPs from the sputter-deposited tri-layers on sapphire (0001) was demonstrated by means of the solid-state dewetting approach. Based on the control of tri-layer thickness, temperature, and deposition order, the alloy NPs were significantly varied in terms of configurations, size, and spatial arrangement. The overall dewetting sequence of as-deposited tri-metallic thin film with 15 nm total thickness exhibited the various steps of dewetting: void initiation, void growth, and cluster breakdown with increasing temperature. With low deposition thickness, i.e., 6 nm, semi-spherical alloy NPs with uniform surface coverage, size, and spatial homogeneity were obtained by the enhanced dewetting of thin tri-layers. On the other hand, the change in disposition order drastically altered the dewetting process under identical growth conditions, in correlation with the distinct binding energy with the substrate and the diffusivity of metals. The formation of composite alloy NPs was attributed to the surface diffusion and inter-mixing of tri-metallic layers by thermal energy and driven by the surface and interface energy minimization to gain equilibrium configuration. Furthermore, Ag sublimation at a relatively high temperature was found to affect the surface morphology and elemental composition of alloy NPs. The optical characterization by reflectance spectra demonstrated a reverse relationship between the average reflectance and the surface coverage of sapphire by alloy NPs, and an absorption band and peaks were formed at specific wavelengths based on the surface morphology, e.g., peaks in the UV and NIR regions and a wide absorption band in the visible region, whereas small NPs (<200 nm) exhibited broadband absorption. The peak intensity showed high dependency on the Ag content of alloy NPs.

Author Contributions: Sundar Kunwar, Puran Pandey, Mao Sui, and Sushil Bastola participated in the experimental design and carried out the experiments. Sundar Kunwar, Puran Pandey, Mao Sui, and Sushil Bastola participated in the data analysis. Sundar Kunwar and Jihoon Lee designed the experiments and testing methods. Sundar Kunwar and Jihoon Lee carried out the writing. All authors helped in drafting and read and approved the final manuscript.

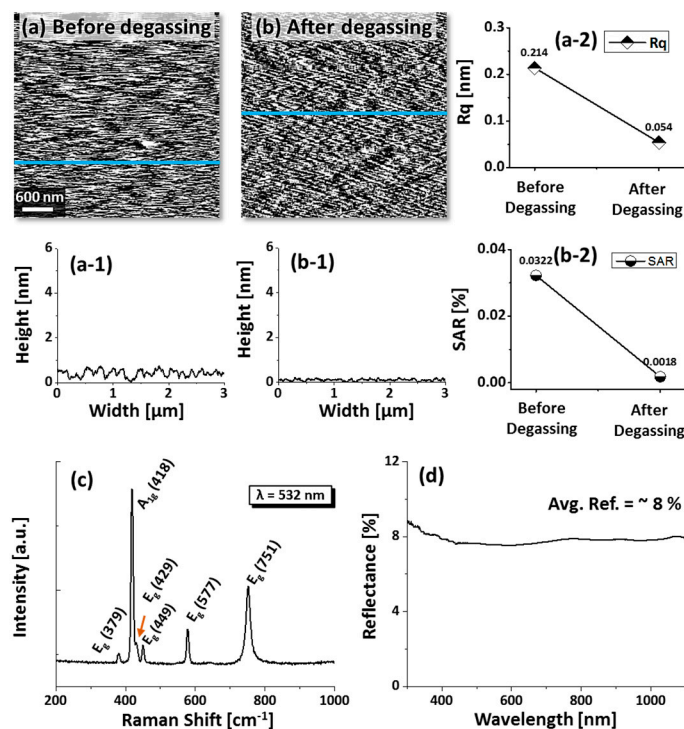**Conflicts of Interest:** The authors declare no conflict of interest.

Appendix A

Figure A1. AFM top-views of bare sapphire (0001) before degassing (**a**) and after degassing (**b**) at 900 °C for 30 min under 1×10^{-6} Torr. (**a-1**–**b-1**) Cross-sectional line profiles depicts the surface texture profile. (**a-2**) Roughness and (**b-2**) surface area ratio (SAR) before and after degassing. (**c**) Raman spectra of the bare sapphire (0001) depicting six natural vibration modes. (**d**) UV-VIS-NIR reflectance spectra of bare sapphire.
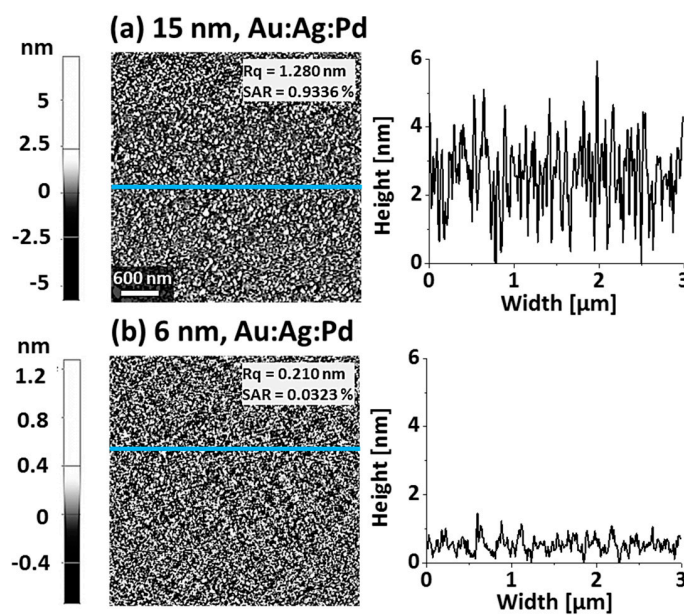

Figure A2. Pre-annealed samples surface morphology after the deposition of Au, Ag, and Pd tri-layer with distinct thickness: (**a**) total thickness of 15 nm with 5 nm of Au, Ag, and Pd in a sequence; (**b**) total thickness of 6 nm with 2 nm of Au, Ag, and Pd in a sequence. The surface morphology depicts higher roughness with 15 nm of thickness, as shown by the cross-sectional line profiles.
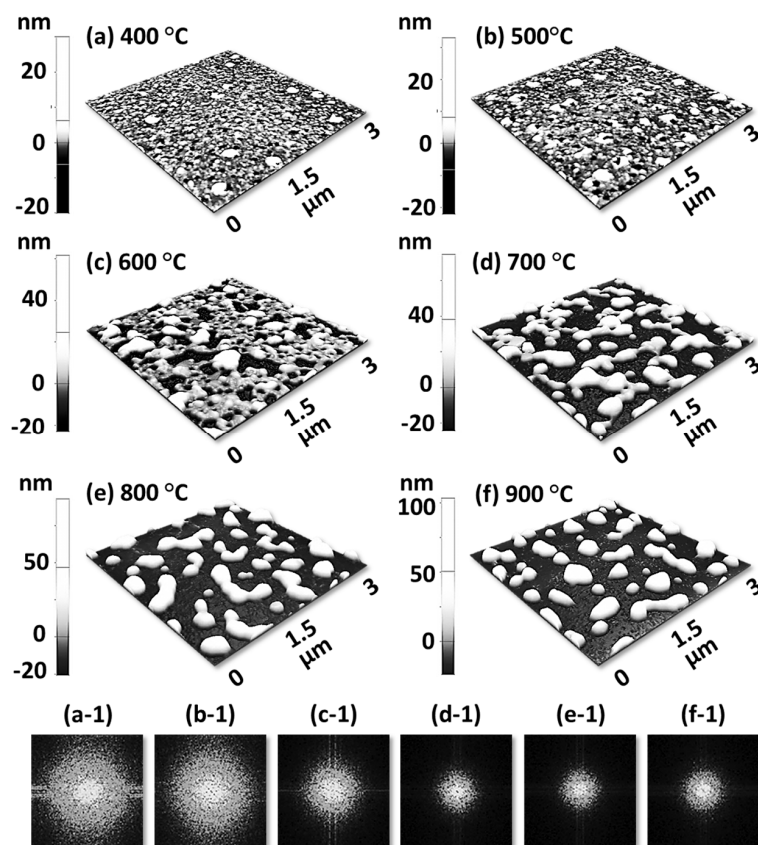
Figure A3. Evolution of dome-shaped AuAgPd alloy NPs from deposited tri-layers of 15 nm total thickness with 2 nm of of Au, Ag, and Pd layers. The fabrication was performed between 400 and 900 °C for constant 450 s. (**a**–**f**) AFM 3D side-views of 3 × 3 μm². (**a-1**–**f-1**) Corresponding FFT power spectra. The circular pattern of FFT spectra gradually reduced with the evolution of alloy NPs denoting the improved overall surface height distribution.
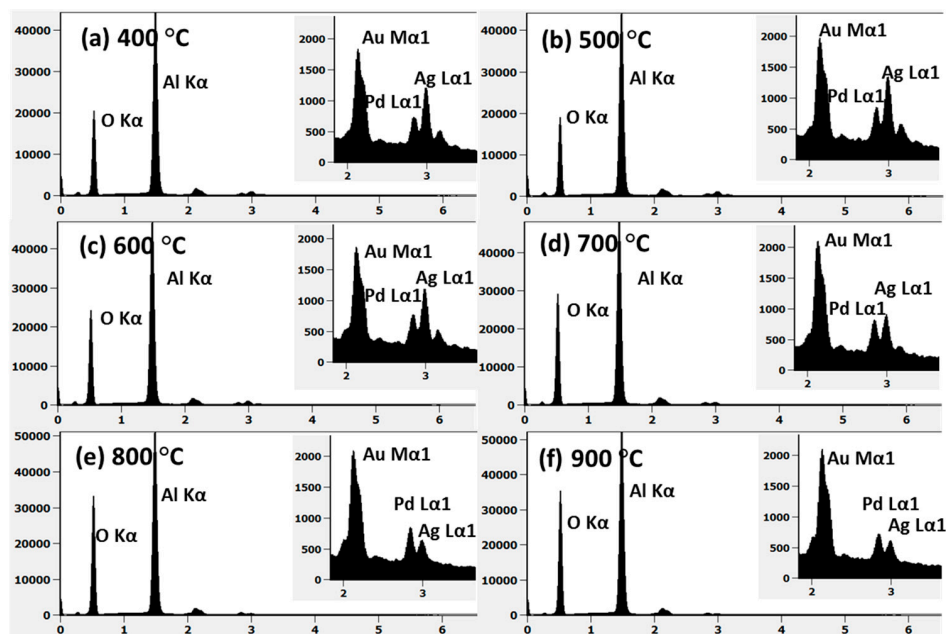

Figure A4. (**a**–**f**) EDS spectra of the AuAgPd alloy NPs on sapphire shown in Figure A3. Insets show the evolution of Au Mα1, Pd Lα1, and Ag Lα1 peaks with annealing temperature.
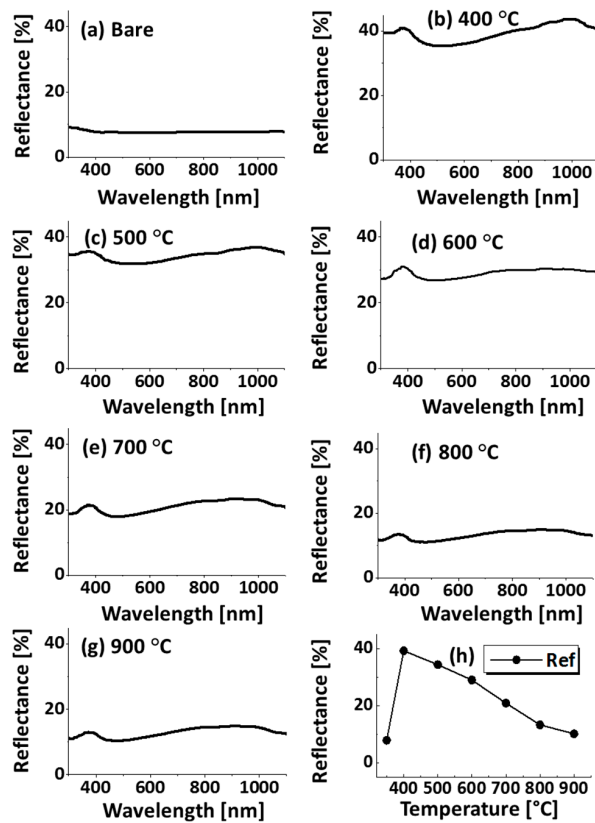
Figure A5. (**a**–**g**) Reflectance spectra of the bare sapphire (0001) and samples shown in Figure A3; (**h**) summary of average reflectance with respect to the temperature.
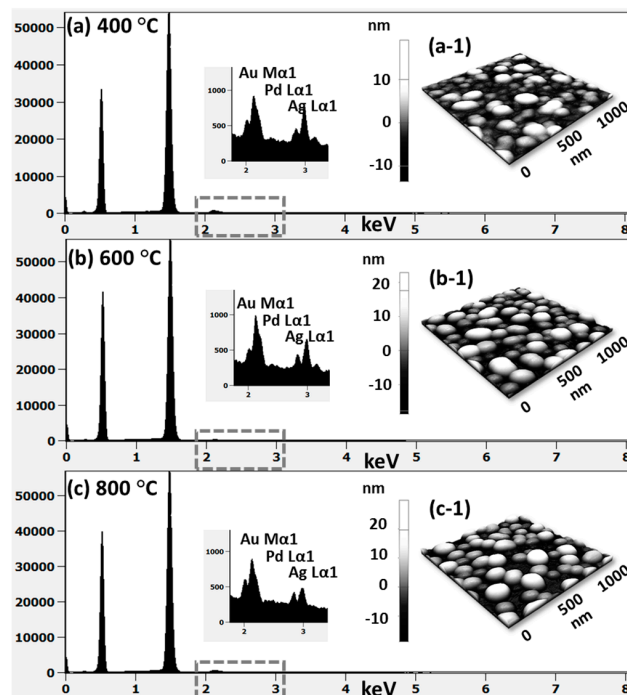

Figure A6. (**a**–**c**) EDS spectra between 0 and 8 keV of the samples with various temperature as labeled. The initial total film thickness was 6 nm with the composition of 2 nm Au, 2 nm Ag, and 2 nm Pd in a sequential order. In sets highlights the Au Mα1, Pd Lα1 and Ag Lα1 peaks of the samples. (**a-1**–**c-1**) Corresponding surface morphologies of the samples with AFM side-views of 1×1 μm^2.
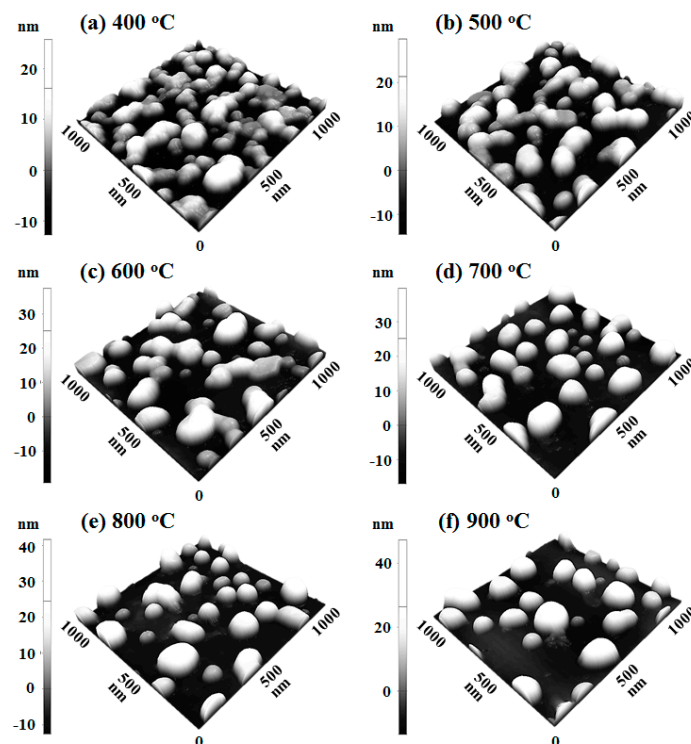
Figure A7. Tri-layer deposition order on the evolution of AuAgPd NPs at increased temperature between 400 and 900 °C. The tri-layers consist of 2 nm thick Pd, Au, and Ag layers in sequence (Pd:Au:Ag = 1:1:1). (**a–f**) AFM side-views of 1×1 μm^2.
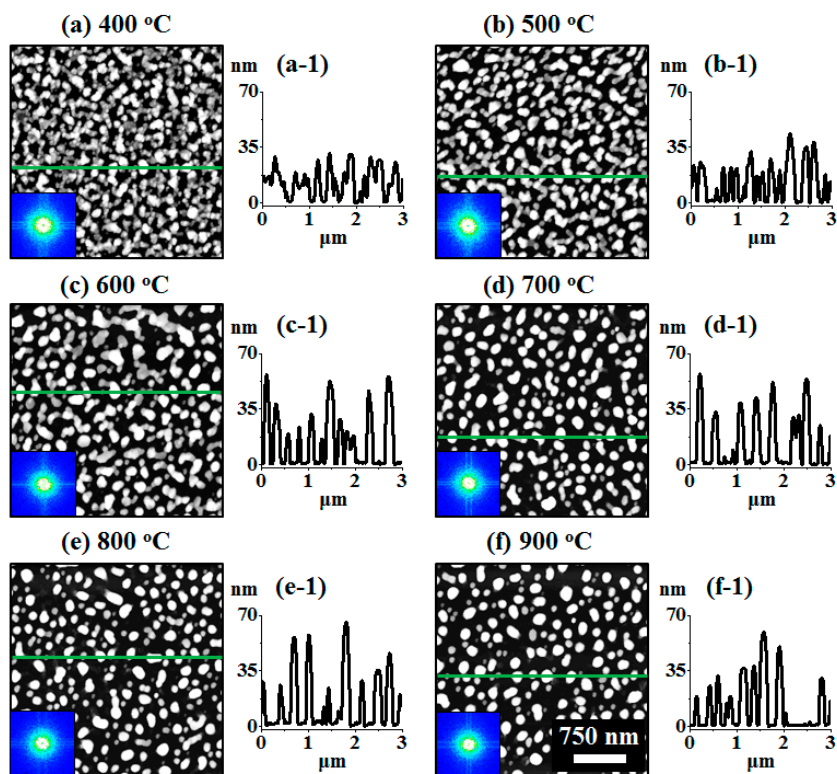

Figure A8. (**a–f**) Large scale AFM top-views of Pd–Au–Ag tri-metallic nanostructures annealed temperature between 400 and 900 °C (Tri-layer of Pd–Au–Ag of total thickness 6 nm and equal composition). (**a-1–f-1**) Cross-sectional line-profiles. Insets in (**a–f**) are FFT power spectra.
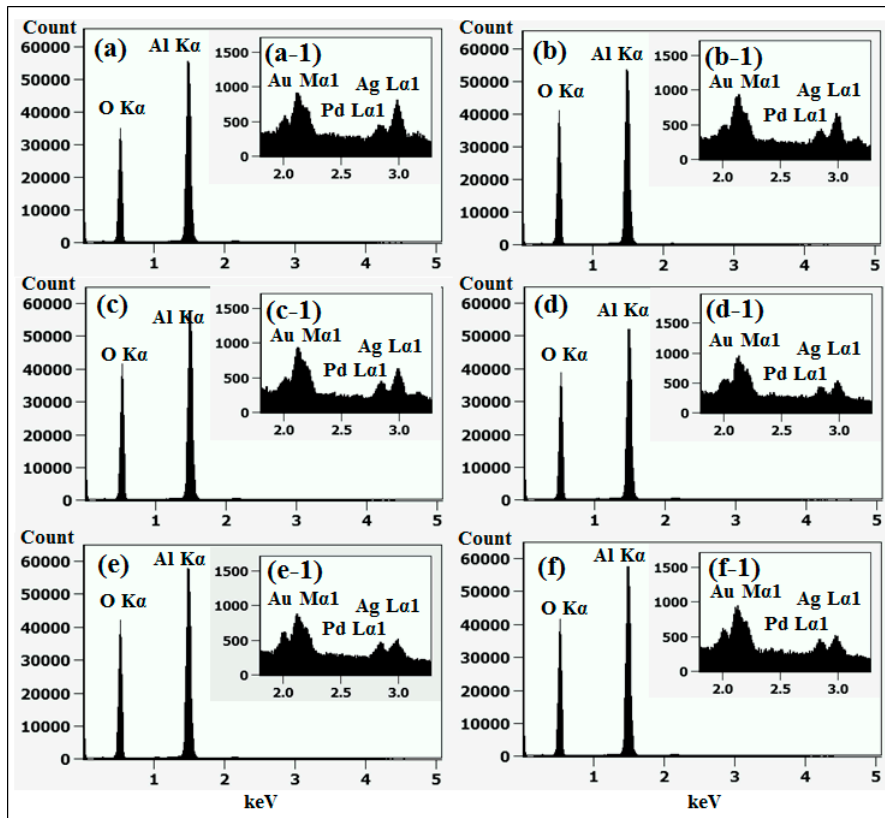
Figure A9. (**a–f**) EDS spectra of various Pd-Au-Ag nanostructures with tri-layer of Pd-Au-Ag of total thickness 6 nm and equal composition followed by annealing between 400 and 900 °C. (**a-1–f-1**) Enlarged EDS spectra.
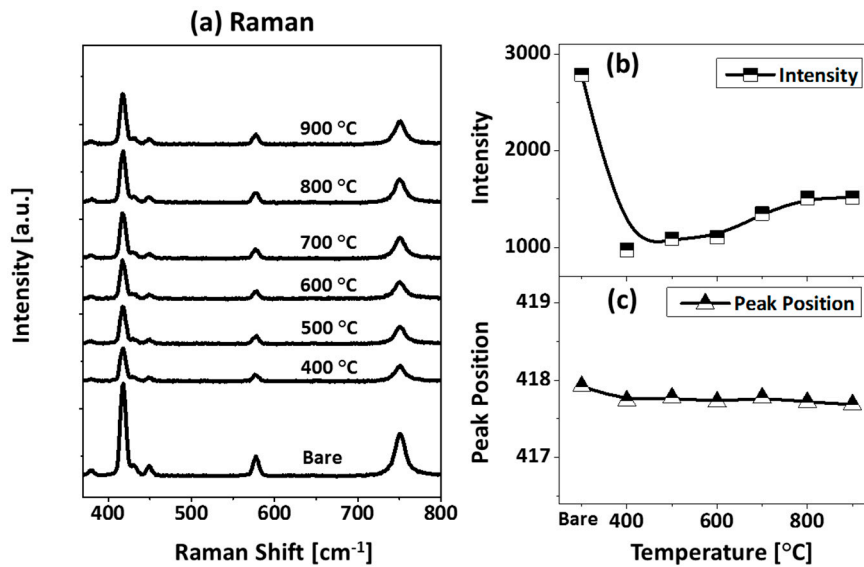

Figure A10. (**a**) Raman spectra of samples shown in Figure A8. (**b**,**c**) Summary plots of intensity and peak position of Raman band A_{1g}.

Table A1. Summary of roughness (Rq), surface area ratio (SAR) of the samples with various deposition amount, composition, and annealing temperature.

Temperature [°C]	Au:Ag:Pd, 15 nm		Au:Ag:Pd, 6 nm		Pd:Au:Ag, 6 nm	
	Rq [nm]	SAR [%]	Rq [nm]	SAR [%]	Rq [nm]	SAR [%]
400	3.18	0.7	5.13	2.86	8.32	7.5
500	4.12	1.25	-	-	10.9	9.98
600	12.32	4.07	9.17	7.07	12.82	11.31
700	21.36	7.38	-	-	12.85	12.04
800	23.58	7.89	9.6	7.32	12.53	10.53
900	25.46	8.88	-	-	13.47	10.98

Table A2. Summary of average reflectance (ref.) of the samples at various temperature, composition, and film thickness.

Temperature [°C]	Au:Ag:Pd, 15 nm	Au:Ag:Pd, 6 nm	Pd:Au:Ag, 6 nm
	Ref. [%]	Ref. [%]	Ref. [%]
Bare	7.821	7.951	7.96
400	39.258	18.629	20.41
500	34.385	-	17.93
600	29.00	15.82	17.09
700	20.870	-	14.50
800	13.246	12.105	12.83
900	10.119	-	11.94

Table A3. Summary of Raman peak intensity and peak position (PP) of the samples with distinct temperature, composition, and thickness.

Temperature [°C]	Au:Ag:Pd, 15 nm		Au:Ag:Pd, 6 nm		Pd:Au:Ag, 6 nm	
	Intensity [a.u.]	PP [cm^{-1}]	Intensity [a.u.]	PP [cm^{-1}]	Intensity [a.u.]	PP [cm^{-1}]
Bare	2711.73	418.67	2583.28	418.52	2786.12	417.91
400	238.90	418.73	987.04	418.28	972.05	417.73
500	251.80	418.39	-	-	1091.37	417.77
600	370.67	418.58	1011.01	418.31	1104.38	417.71
700	729.88	418.62	-	-	1348.80	417.77
800	1024.83	418.54	1561.28	418.39	1510.26	417.72
900	1220.36	418.49	-	-	1511.32	417.68

Table A4. Summary of average diameter (AD) and average height (AH) of the samples at distinct annealing temperature and composition.

Temperature [°C]	Au:Ag:Pd, 6 nm		Pd:Au:Ag, 6 nm
	AD [nm]	AH [nm]	AH [nm]
400	115.54	14.17	24.29
500	-	-	27.42
600	140.43	27.53	31.99
700	-	-	34.25
800	141.16	27.74	31.77
900	-	-	37.08

References

1. Kim, H.-J.; Jung, S.C.; Han, Y.-K.; Oh, S.H. An atomic-level strategy for the design of a low overpotential catalyst for Li–O$_2$ batteries. *Nano Energy* **2015**, *13*, 679–686. [CrossRef]

2. Olmos, C.M.; Chinchilla, L.E.; Rodrigues, E.G.; Delgado, J.J.; Hungría, A.B.; Blanco, G.; Pereira, M.F.R.; Órfão, J.J.M.; Calvino, J.J.; Chen, X. Synergistic effect of bimetallic Au-Pd supported on ceria-zirconia mixed oxide catalysts for selective oxidation of glycerol. *Appl. Catal. B Environ.* **2016**, *197*, 222–235. [CrossRef]

3. Zhao, B.; Zhao, W.; Shao, G.; Fan, B.; Zhang, R. Morphology-control synthesis of a core-shell structured NiCu alloy with tunable electromagnetic-wave absorption capabilities. *ACS Appl. Mater. Interfaces* **2015**, *7*, 12951–12960. [CrossRef] [PubMed]

4. Macarena, M.; Ponce, S.; Zhang, G.-R.; Etzold, B.J.M. Size-controlled PtNi nanoparticles as highly efficient catalyst for hydrodechlorination reactions. *Appl. Catal. B Environ.* **2016**, *192*, 1–7.

5. Kang, M.; Park, S.-G.; Jeong, K.-H. Repeated solid-state dewetting of thin gold films for nanogap-rich plasmonic nanoislands. *Sci. Rep.* **2015**, *5*, 14790. [CrossRef] [PubMed]

6. Huang, Y.; Zhang, Y.; Chen, X.; Wu, D.; Yi, Z.; Cao, R. Bimetallic alloy nanocrystals encapsulated in ZIF-8 for synergistic catalysis of ethylene oxidative degradation. *Chem. Commun.* **2014**, *50*, 10115–10117. [CrossRef] [PubMed]

7. Müller, M.B.; Kuttner, C.; König, T.A.; Tsukruk, V.V.; Förster, S.; Karg, M.; Fery, A. Plasmonic library based on substrate-supported gradiential plasmonic arrays. *ACS Nano* **2014**, *8*, 9410–9421. [CrossRef] [PubMed]

8. Zhao, W.; Wang, S.; Liu, B.; Verzhbitskiy, I.; Li, S.; Giustiniano, F.; Kozawa, D.; Loh, K.P.; Matsuda, K.; Okamoto, K.; et al. Exciton-plasmon coupling and electromagnetically induced transparency in monolayer semiconductors hybridized with ag nanoparticles. *Adv. Mater.* **2016**, *28*, 2709–2715. [CrossRef] [PubMed]

9. He, Q.; Miedziak, P.J.; Kesavan, L.; Dimitratos, N.; Sankar, M.; Lopez-Sanchez, J.A.; Forde, M.M.; Edwards, J.K.; Knight, D.W.; Taylor, S.H.; et al. Switching-off toluene formation in the solvent-free oxidation of benzyl alcohol using supported trimetallic Au–Pd–Pt nanoparticles. *Faraday Discuss.* **2013**, *162*, 365–378. [CrossRef] [PubMed]

10. Tiruvalam, R.C.; Pritchard, J.C.; Dimitratos, N.; Lopez-Sanchez, J.A.; Edwards, J.K.; Carley, A.F.; Hutchings, G.J.; Kiely, C.J. Aberration corrected analytical electron microscopy studies of sol-immobilized Au+ Pd, Au {Pd} and Pd {Au} catalysts used for benzyl alcohol oxidation and hydrogen peroxide production. *Faraday Discuss.* **2011**, *152*, 63–86. [CrossRef] [PubMed]

11. He, C.; Tao, J.; He, G.; Shen, P.K.; Qiu, Y. Unravelling the promoting effect of the ultrathin TaC/RGO nanosheet hybrid for enhanced catalytic activity of Pd nanoparticles. *Catal. Sci. Technol.* **2016**, *6*, 7086–7093. [CrossRef]

12. Saha, S.; Vaidya, S.; Ramanujachary, K.V.; Lofland, S.E.; Ganguli, A.K. Ternary alloy nanocatalysts for hydrogen evolution reaction. *Bull. Mater. Sci.* **2016**, *39*, 433–436. [CrossRef]

13. Su, R.; Tiruvalam, R.; Logsdail, A.J.; He, Q.; Downing, C.A.; Jensen, M.T.; Dimitratos, N.; Kesavan, L.; Wells, P.P.; Bechstein, R.; et al. Designer titania-supported Au–Pd nanoparticles for efficient photocatalytic hydrogen production. *ACS Nano* **2014**, *8*, 3490–3497. [CrossRef] [PubMed]

14. Jongsomjit, S.; Prapainainar, P.; Sombatmankhong, K. Synthesis and characterisation of Pd–Ni–Sn electrocatalyst for use in direct ethanol fuel cells. *Solid State Ion.* **2016**, *288*, 147–153. [CrossRef]

15. Mohanraju, K.; Cindrella, L. One-pot surfactant-free synthesis of high surface area ternary alloys, PtMCo/C (M= Cr, Mn, Fe, Ni, Cu) with enhanced electrocatalytic activity and durability for PEM fuel cell application. *Int. J. Hydrogen Energy* **2016**, *41*, 9320–9331. [CrossRef]

16. Chokprasombat, K.; Pinitsoontorn, S.; Maensiri, S. Effects of Ni content on nanocrystalline Fe–Co–Ni ternary alloys synthesized by a chemical reduction method. *J. Magn. Magn. Mater.* **2016**, *405*, 174–180. [CrossRef]

17. Li, M.-Y.; Sui, M.; Pandey, P.; Zhang, Q.-Z.; Kunwar, S.; Salamo, G.J.; Lee, J. Precise control of configuration, size and density of self-assembled Au nanostructures on 4H-SiC (0001) by systematic variation of deposition amount, annealing temperature and duration. *CrystEngComm* **2016**, *18*, 3347–3357. [CrossRef]

18. Wang, D.; Liu, S.; Wang, J.; Lin, R.; Kawasaki, M.; Rus, E.; Silberstein, K.E.; Lowe, M.A.; Lin, F.; Nordlund, D.; et al. Spontaneous incorporation of gold in palladium-based ternary nanoparticles makes durable electrocatalysts for oxygen reduction reaction. *Nat. Commun.* **2016**, *7*, 11941. [CrossRef] [PubMed]

19. Chen, J.; Wiley, B.; McLellan, J.; Xiong, Y.; Li, Z.-Y.; Xia, Y. Optical properties of Pd–Ag and Pt–Ag nanoboxes synthesized via galvanic replacement reactions. *Nano Lett.* **2005**, *5*, 2058–2062. [CrossRef] [PubMed]

20. Venkatesan, P.; Santhanalakshmi, J. Designed synthesis of Au/Ag/Pd trimetallic nanoparticle-based catalysts for Sonogashira coupling reactions. *Langmuir* **2010**, *26*, 12225–12229. [CrossRef] [PubMed]

21. Zhou, L.; Liu, Z.; Zhang, H.; Cheng, S.; Fan, L.J.; Ma, W. Site-specific growth of AgPd nanodendrites on highly purified Au bipyramids with remarkable catalytic performance. *Nanoscale* **2014**, *6*, 12971–12980. [CrossRef] [PubMed]

22. Han, Q.; Zhang, C.; Gao, W.; Han, Z.; Liu, T.; Li, C.; Wang, Z.; He, E.; Zheng, H. Ag-Au alloy nanoparticles: Synthesis and in situ monitoring SERS of plasmonic catalysis. *Sens. Actuators B Chem.* **2016**, *231*, 609–614. [CrossRef]

23. Oh, Y.-J.; Kim, J.-H.; Thompson, C.V.; Ross, C.A. Templated assembly of Co–Pt nanoparticles via thermal and laser-induced dewetting of bilayer metal films. *Nanoscale* **2013**, *5*, 401–407. [CrossRef] [PubMed]

24. Pandey, P.; Sui, M.; Li, M.-Y.; Zhang, Q.; Kim, E.-S.; Lee, J. Systematic Study on the Self-Assembled Hexagonal Au Voids, Nano-Clusters and Nanoparticles on GaN (0001). *PLoS ONE* **2015**, *10*, e0134637. [CrossRef] [PubMed]

25. Esterina, R.; Liu, X.M.; Adeyeye, A.O.; Ross, C.A.; Choi, W.K. Solid-state dewetting of magnetic binary multilayer thin films. *J. Appl. Phys.* **2015**, *118*, 144902. [CrossRef]

26. Nanda, K.K.; Sahu, S.N.; Behera, S.N. Liquid-drop model for the size-dependent melting of low-dimensional systems. *Phys. Rev. A* **2002**, *66*, 90–95. [CrossRef]

27. Kunwar, S.; Sui, M.; Pandey, P.; Zhang, Q.; Li, M.-Y.; Bhandari, H.; Lee, J. Determination of growth regimes of Pd nanostructures on c-plane sapphire by the control of deposition amount at different annealing temperatures. *Phys. Chem. Chem. Phys.* **2017**, *19*, 15084–15097. [CrossRef] [PubMed]

28. Wang, D.; Schaaf, P. Solid-state dewetting for fabrication of metallic nanoparticles and influences of nanostructured substrates and dealloying. *Phys. Status Solidi* **2013**, *210*, 1544–1551. [CrossRef]

29. Kunwar, S.; Sui, M.; Zhang, Q.; Pandey, P.; Li, M.-Y.; Lee, J. Various silver nanostructures on sapphire using plasmon self-assembly and dewetting of thin films. *Nano-Micro Lett.* **2017**, *9*, 17. [CrossRef]

30. Müller, C.M.; Spolenak, R. Dewetting of Au and AuPt alloy films: A dewetting zone model. *J. Appl. Phys.* **2013**, *113*, 094301. [CrossRef]

31. Nugroho, F.A.; Iandolo, B.; Wagner, J.B.; Langhammer, C. Bottom-up nanofabrication of supported noble metal alloy nanoparticle arrays for plasmonics. *ACS Nano* **2016**, *10*, 2871–2879. [CrossRef] [PubMed]

32. Kovalenko, O.; Greer, J.R.; Rabkin, E. Solid-state dewetting of thin iron films on sapphire substrates controlled by grain boundary diffusion. *Acta Mater.* **2013**, *61*, 3148–3156. [CrossRef]

33. Klinger, L.; Amram, D.; Rabkin, E. Kinetics of a retracting solid film edge: The case of high surface anisotropy. *Scr. Mater.* **2011**, *64*, 962–965. [CrossRef]

34. Kim, G.H.; Thompson, C.V. Effect of surface energy anisotropy on Rayleigh-like solid-state dewetting and nanowire stability. *Acta Mater.* **2015**, *84*, 190–201. [CrossRef]

35. Xue, L.; Han, Y. Inhibition of dewetting of thin polymer films. *Prog. Mater. Sci.* **2012**, *57*, 947–979. [CrossRef]

36. Ruffino, F. Experimental Analysis on the Molten-Phase Dewetting Characteristics of AuPd Alloy Films on Topographically-Structured Substrates. *Metals* **2017**, *7*, 327. [CrossRef]

37. Yang, L.; Li, X.; Tuo, X.; Nguyen, T.T.V.; Luo, X.; Hong, M. Alloy nanoparticle plasmon resonance for enhancing broadband antireflection of laser-textured silicon surfaces. *Opt. Express* **2011**, *19*, A657–A663. [CrossRef] [PubMed]

38. Saini, C.P.; Barman, A.; Kumar, M.; Satpati, B.; Som, T.; Kanjilal, A. Self-decorated Au nanoparticles on antireflective Si pyramids with improved hydrophobicity. *J. Appl. Phys.* **2016**, *119*, 134904. [CrossRef]

39. Leong, K.H.; Chu, H.Y.; Ibrahim, S.; Saravanan, P. Palladium nanoparticles anchored to anatase TiO$_2$ for enhanced surface plasmon resonance-stimulated, visible-light-driven photocatalytic activity. *Beilstein J. Nanotechnol.* **2015**, *6*, 428–437. [CrossRef] [PubMed]

40. Kadleıková, M.; Breza, J.; Veselý, M. Raman spectra of synthetic sapphire. *Microelectron. J.* **2001**, *32*, 955–958. [CrossRef]

41. Kuball, M. Raman spectroscopy of GaN, AlGaN and AlN for process and growth monitoring/control. *Surf. Interface Anal.* **2001**, *31*, 987–999. [CrossRef]

42. Guidelli, E.J.; Baffa, O.; Clarke, D.R. Enhanced UV emission from silver/ZnO and gold/ZnO core-shell nanoparticles: Photoluminescence, radioluminescence, and optically stimulated luminescence. *Sci. Rep.* **2015**, *5*, 14004. [CrossRef] [PubMed]

43. Sadan, H.; Kaplan, W.D. Au–Sapphire (0001) solid–solid interfacial energy. *J. Mater. Sci.* **2006**, *41*, 5099–5107. [CrossRef]

44. Højrup, H.K.; Worren, T.; Stempel, S.; Lægsgaard, E.; Bäumer, M.; Freund, H.-J.; Besenbacher, F.; Stensgaard, I. Palladium nanocrystals on Al_2O_3: Structure and adhesion energy. *Phys. Rev. Lett.* **1999**, *83*, 4120–4123.